Supplemental Material for "Biomass-burning-derived particles from a wide variety of fuels: Part 2: Effects of photochemical aging on particle optical and chemical properties"

Christopher D. Cappa[1,2,*], Christopher Y. Lim[3], David H. Hagan[3], Matthew Coggon[4,5,7], Abigail Koss[4,5^], Kanako Sekimoto[4,5,6], Joost de Gouw[5,7], Timothy B. Onasch[8], Carsten Warneke,[4,5] Jesse H. Kroll[3]

[1] Department of Civil and Environmental Engineering, University of California, Davis, CA, USA 95616

[2] Atmospheric Sciences Graduate Group, University of California, Davis, CA, USA 95616

[3] Department of Civil and Environmental Engineering, Massachusetts Institute of Technology, Cambridge, MA, USA

[4] NOAA Earth System Research Laboratory (ESRL), Chemical Sciences Division, Boulder, CO 80305, USA

[5] Cooperative Institute for Research in Environmental Sciences, University of Colorado Boulder, Boulder, CO 80309, USA

[6] Graduate School of Nanobioscience, Yokohama City University, Yokohama, Kanagawa 236-0027, Japan

[7] Department of Chemistry, University of Colorado Boulder, Boulder, CO 80302, USA

[8] Aerodyne Research, Billerica, MA 01821, USA

[^] Now at Department of Civil and Environmental Engineering, Massachusetts Institute of Technology, Cambridge, MA, USA

[*] To whom correspondence should be addressed: cdcappa@ucdavis.edu

1 Supplementary Material

1.1 Model parameter cross-sensitivities and uncertainties

The SOA yields are most sensitive to the initial [NMOG]/[OA] ratio. When the [NMOG]/[OA] ratio is assumed larger, the necessary SOA yields are smaller. There is an approximately inverse relationship between the assumed initial [NMOG] and the SOA yield for each NMOG type (fast, slow, very slow). However, the influence of multi-generational impacts the relationship to some extent.

The O:C ratios for the different SOA types are weakly dependent on the relative abundances specified for the different types. There is also a weak cross-sensitivity between the O:C values specified for the different SOA types, especially between the fast and slow-forming SOA. In general, if the $O:C_{fast}$ is increased, the $O:C_{slow}$ must be decreased. However, only relatively minor variations in the O:C of each type is allowable to obtain reasonable model-measurement agreement, especially at short photochemical ages. The f_{60} values for the different SOA types exhibit similar cross-sensitivities as the O:C values. However, they are generally less sensitive, in comparison, because the f_{60} values are so similar for all SOA types.

The model k_{OH} values also exhibit some dependence on the assumed initial [NMOG]/[OA] and yields. In general, if $k_{OH,fast}$ is decreased the $k_{OH,slow}$ must be increased. However, the $k_{OH,fast}$ is reasonably well-constrained by the rapid rise in the [OA]/[rBC] and O:C for all particle classes, and by the increase in the $MAC_{BrC,405nm}$ that is observed at very short photochemical ages for some of the particle classes. The assumed k_{OH} for multi-generational aging is most sensitive to the choice of the $k_{OH,slow}$, with the two generally exhibiting an inverse relationship.

It is difficult to estimate a comprehensive uncertainty on these values; we qualitatively estimate uncertainties based on the model sensitivity to changing these parameter values. If the MAC_{fast} were as small as the values for the other SOA types the modeled MAC_{BrC} would decline much too rapidly compared to the observations. Also, it is necessary that the MAC_{fast} be greater than the MAC_{BrC} of the primary OA for SSA class 5 and class 6 to reproduce the initial increase at short aging times. However, if the MAC_{fast} were much larger than our estimate the model predicts an initial increase in the MAC_{BrC} for the intermediate SSA classes 3 and 4, in contrast to the observations. We therefore estimate a uncertainty of $\pm$ 0.2 $m^2 g^{-1}$ based on the model sensitivity to variations in this parameter. The MAC_{slow} values are largely determined by the behavior at intermediate equivalent ages, as this is where they have the largest fractional contributions; we estimate the uncertainty as ± 0.05 m^2 g^{-1}. The MAC_{VS} is not especially well-constrained as it only makes up a very small fraction of the OA mass. A value of MAC_{VS} = 0.05 m^2 s^{-1} is used for consistency with the MAC_{slow}, but a value of MAC_{VS} = 0 m^2 g^{-1}, i.e. non-absorbing, is not entirely unreasonable. The MAC_{2G} and MAC_{het} values are primarily determined by the behavior at long equivalent ages. The estimated uncertainty in MAC_{2G} is ± 0.05 m^2 g^{-1} while the estimated uncertainty in MAC_{het} is ± 0.025 m^2 g^{-1}. That the MAC_{het} is smaller than the MAC_{BrC} values for the various SOA types indicates that over longer time the overall MAC_{BrC} will continue to decline until it reaches 0.05 m^2 g^{-1}.

1.2 Supplemental Figures

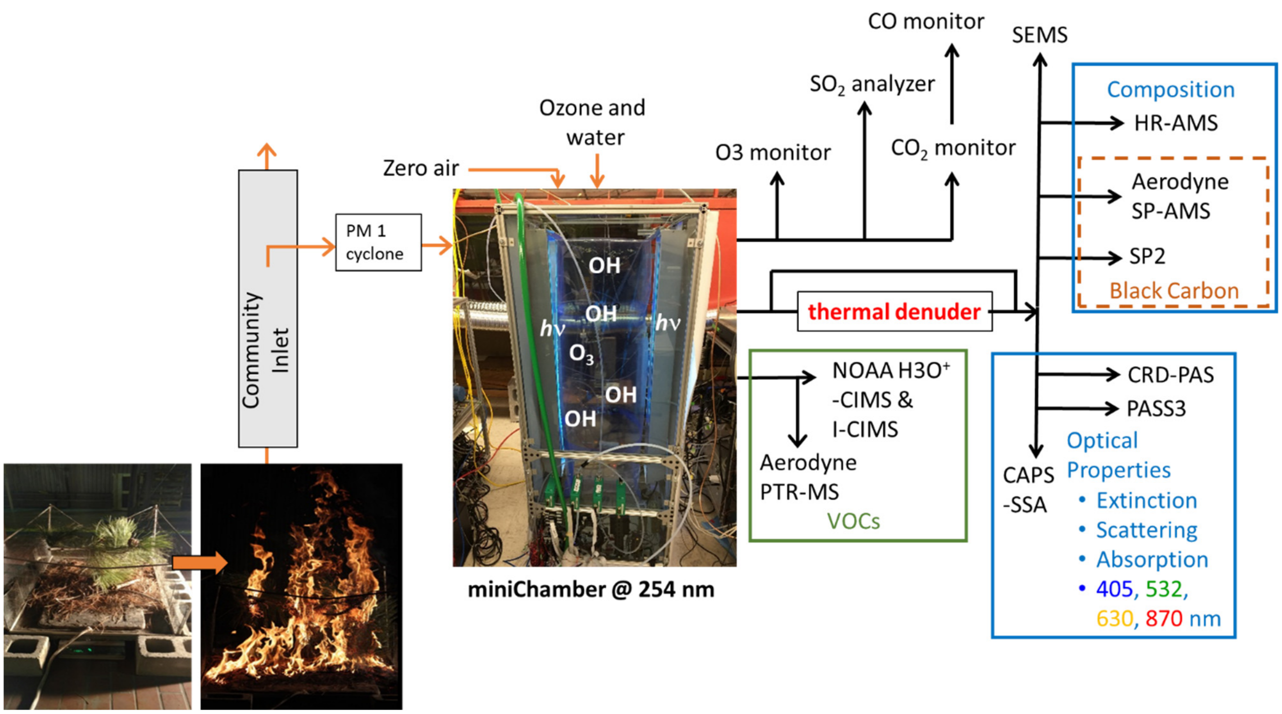

Figure S1. Cartoon schematic of sampling into and from the mini chamber during FIREX. Instrument names are given in

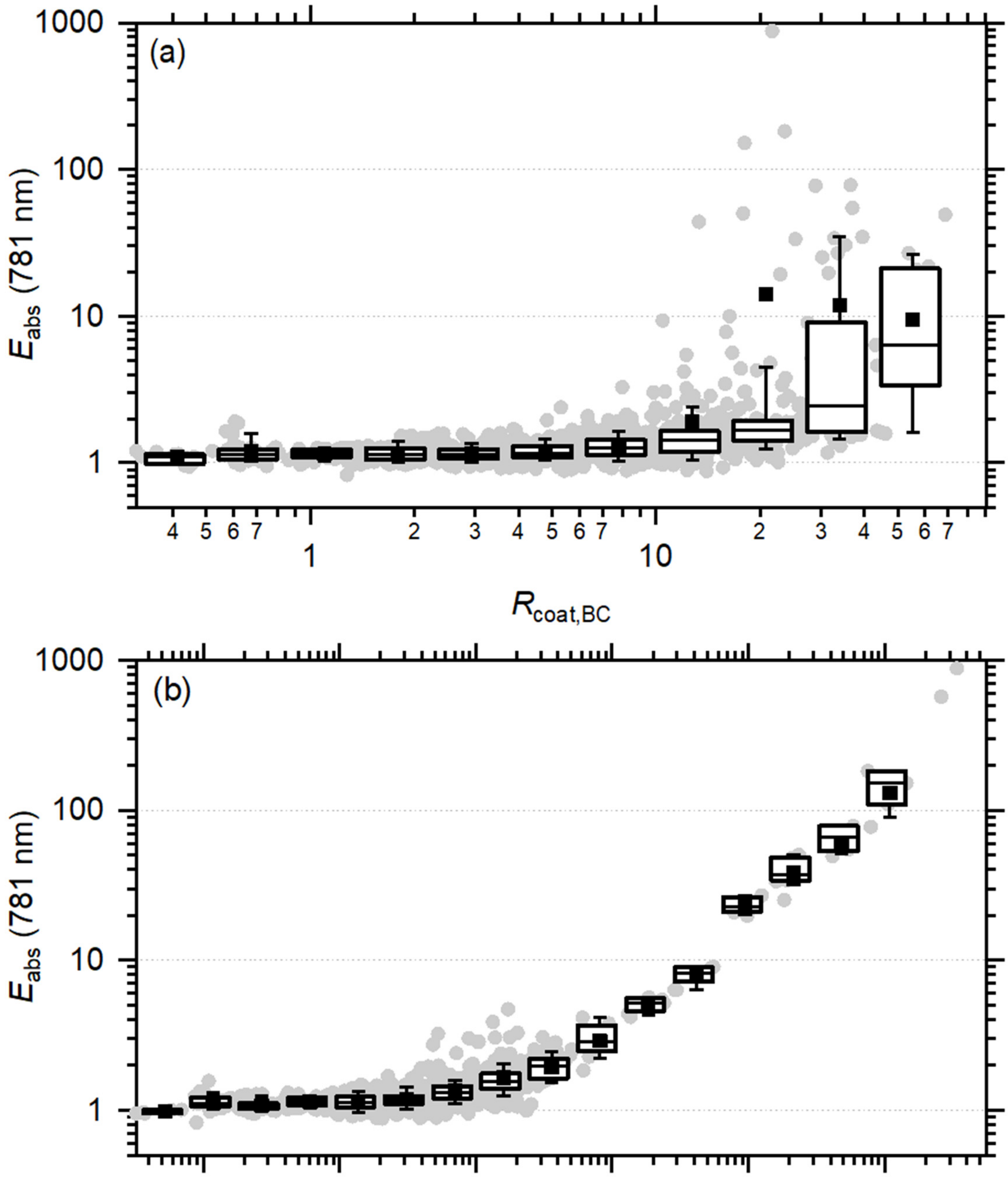

Figure S2. (a) Dependence of the observed E_{abs} 781 nm on the coating-to-rBC core mass ratio, $R_{coat\text{-}rBC}$. (b) Dependence of the E_{abs} at 781 nm on the [NR-PM]/[rBC] ratio. The observations have been binned according to either the $R_{coat\text{-}rBC}$ or [NR-PM]/[rBC] ratio, shown as box-and-whisker plots.

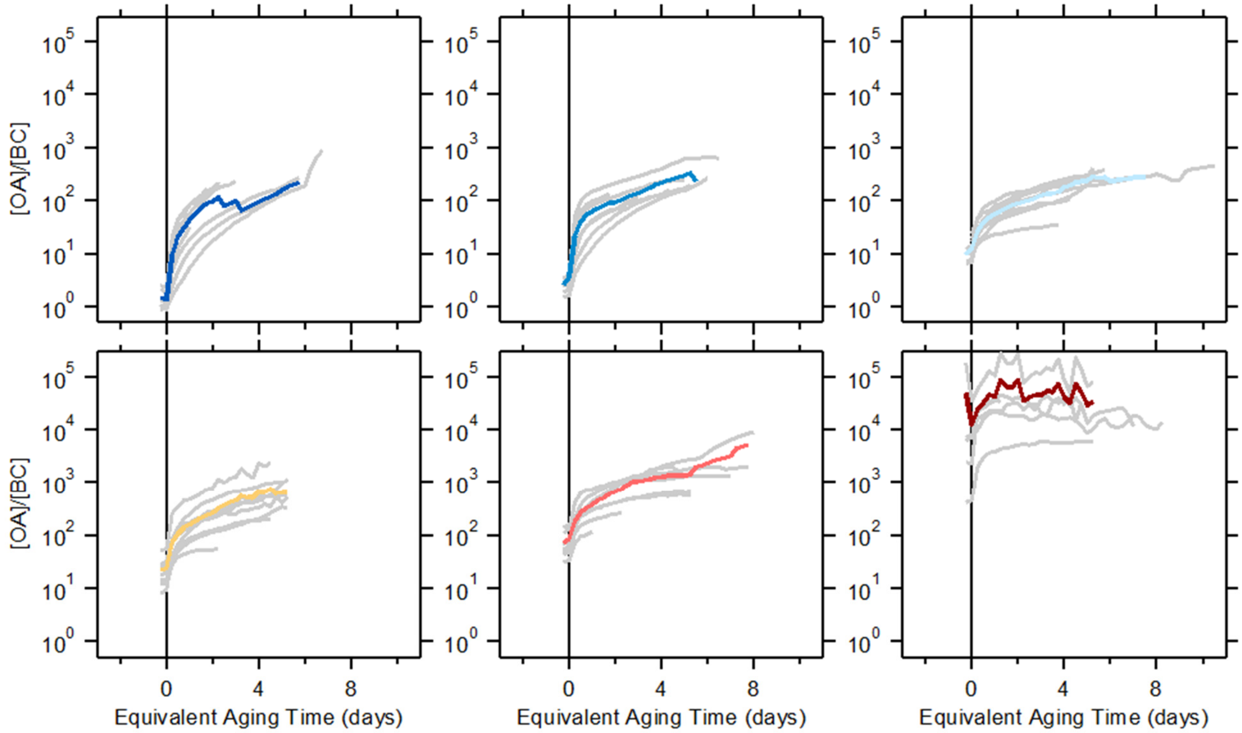

Figure S3. Relationship between [OA]/[BC] and the equivalent atmospheric aging time for each SSA classification. Individual burns are shown as gray lines, and the average for each SSA class as the colored line.

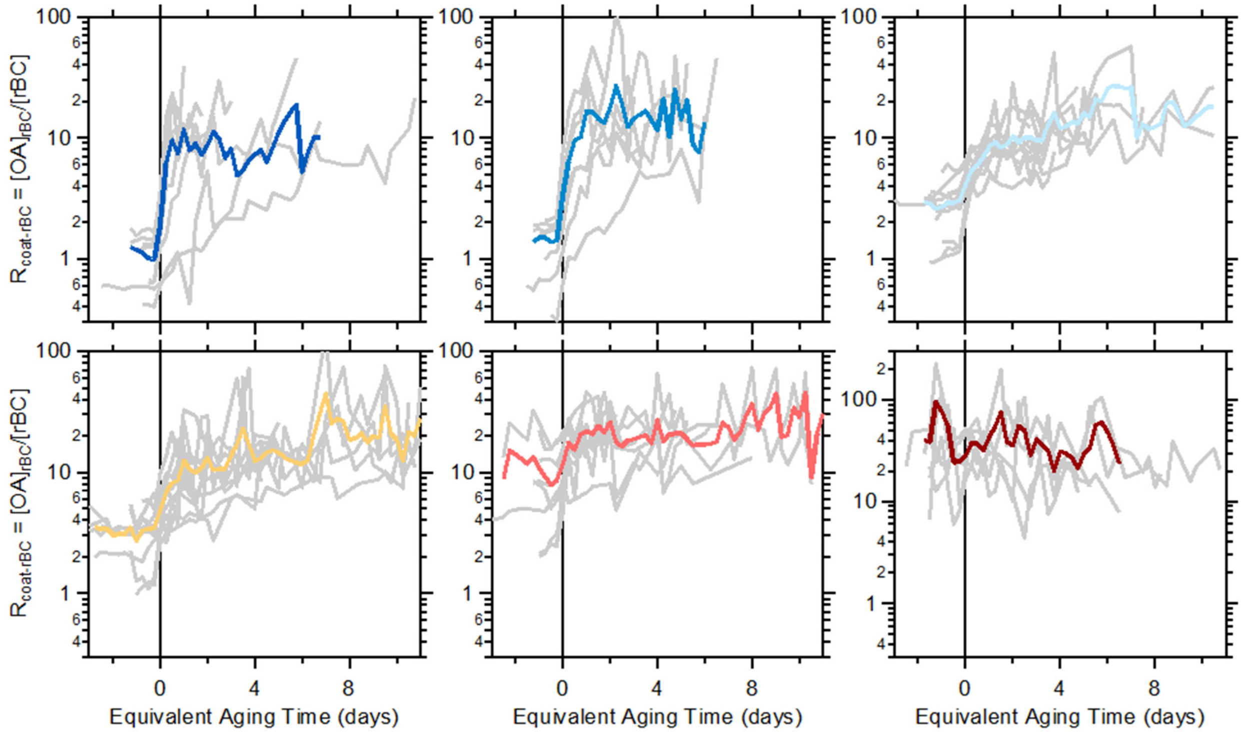

Figure S4. Relationship between $R_{\text{coat-rBC}}$ and the equivalent atmospheric aging time for each SSA classification. Individual burns are shown as gray lines, and the average for each SSA class as the colored line.

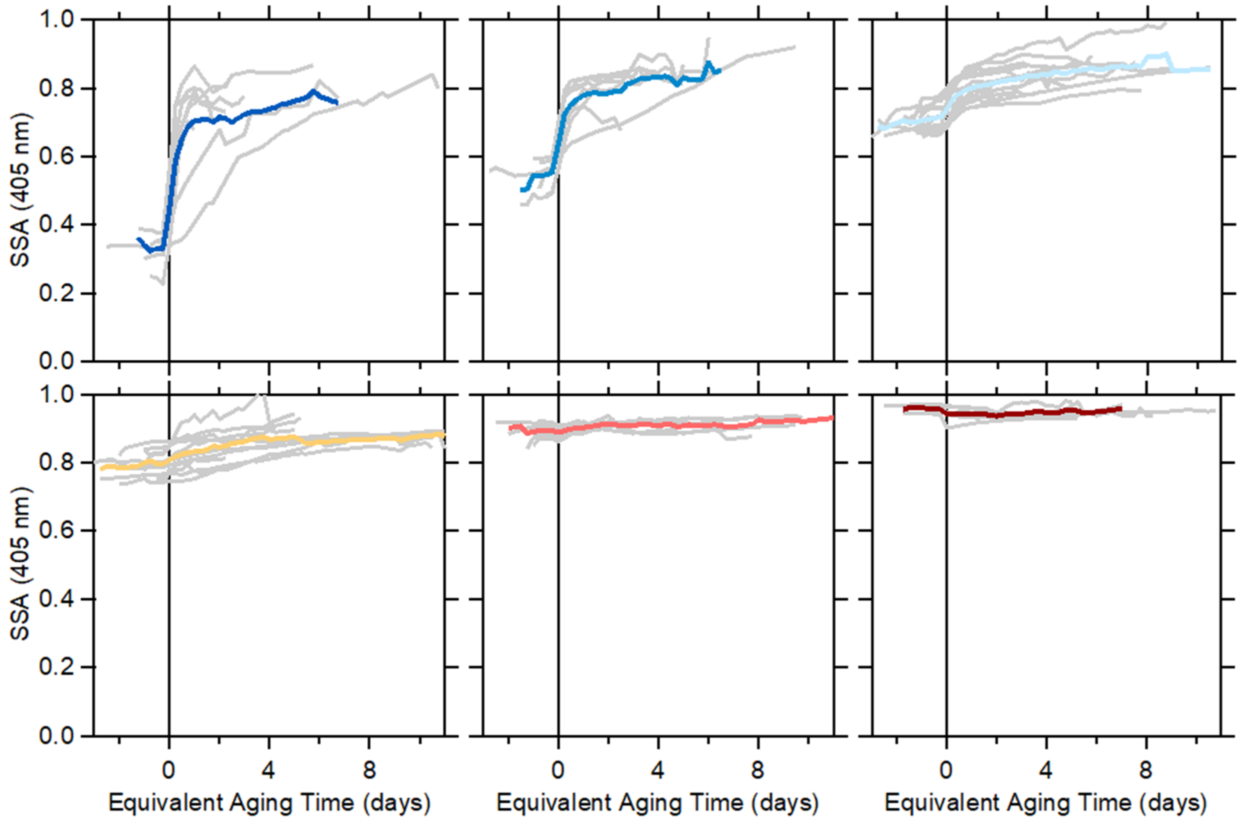

Figure S5. Relationship between SSA at 405 nm and the equivalent atmospheric aging time for each SSA classification. Individual burns are shown as gray lines, and the average for each SSA class as the colored line.

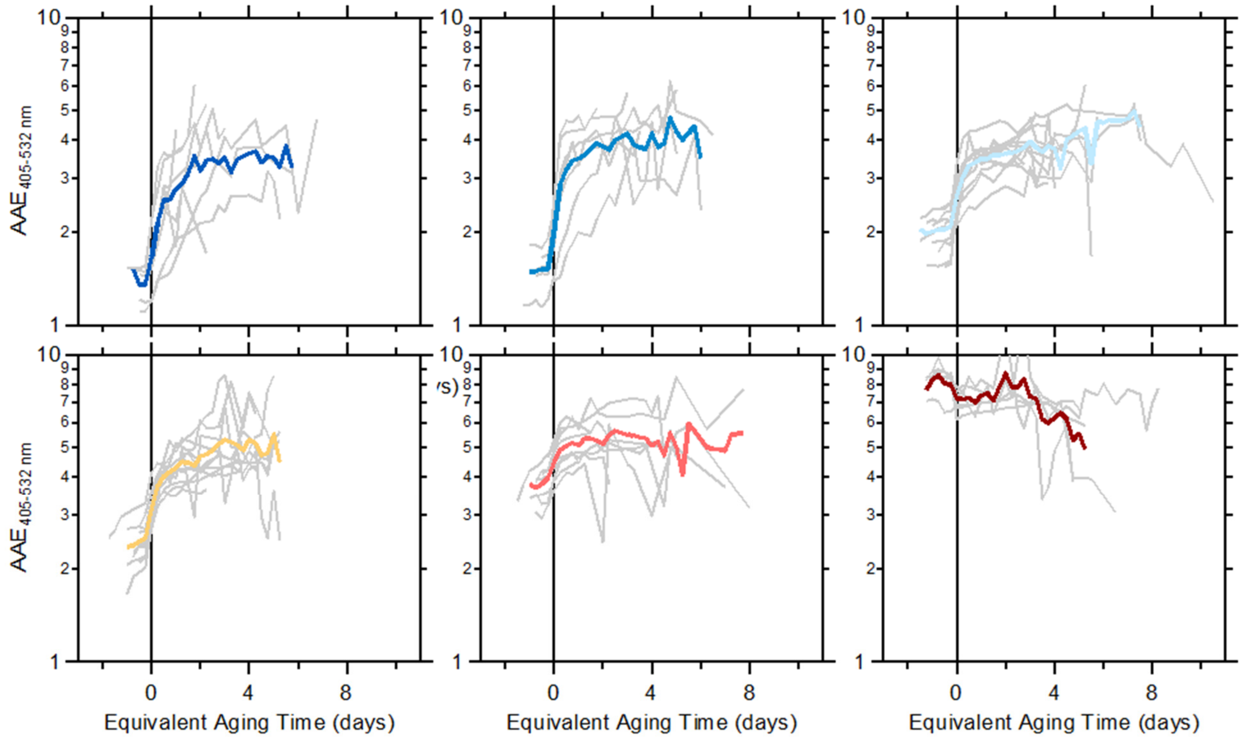

Figure S6. Relationship between the $AAE_{405-532}$ and the equivalent atmospheric aging time for each SSA classification. Individual burns are shown as gray lines, and the average for each SSA class as the colored line.

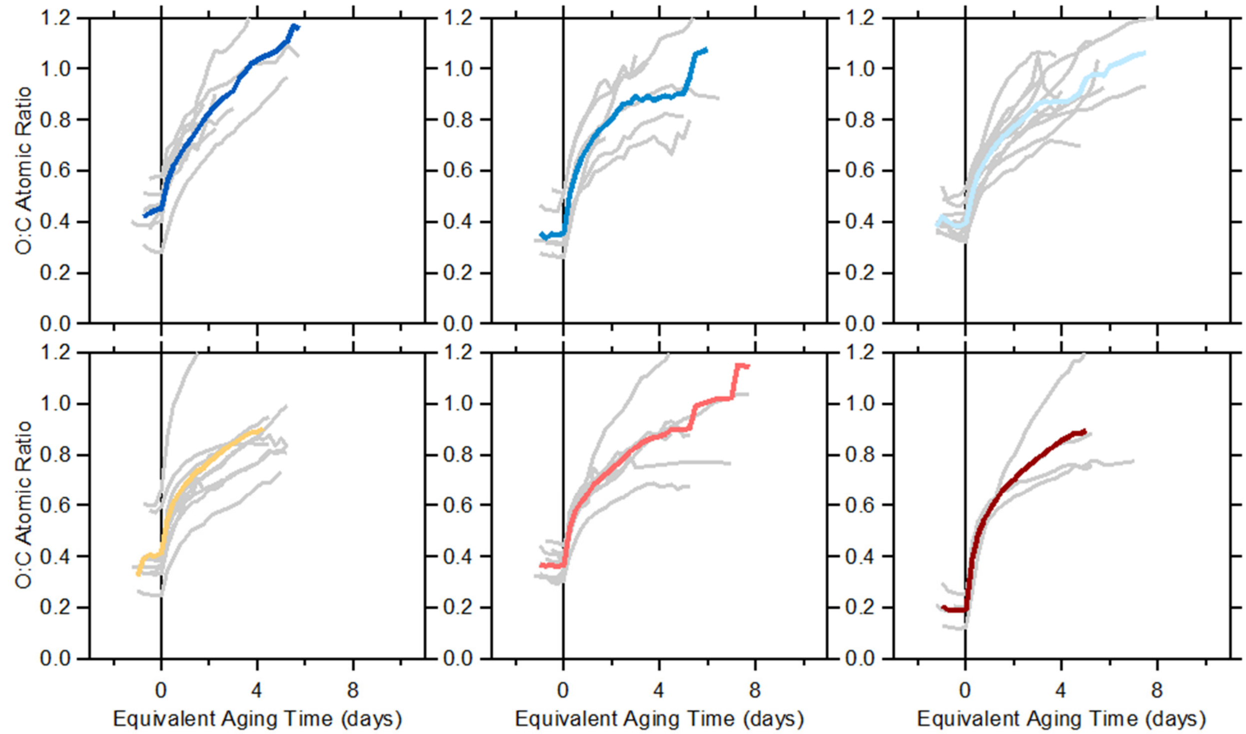

Figure S7. Relationship between the O:C atomic ratio at 405 nm and the equivalent atmospheric aging time for each SSA classification. Individual burns are shown as gray lines, and the average for each SSA class as the colored line.

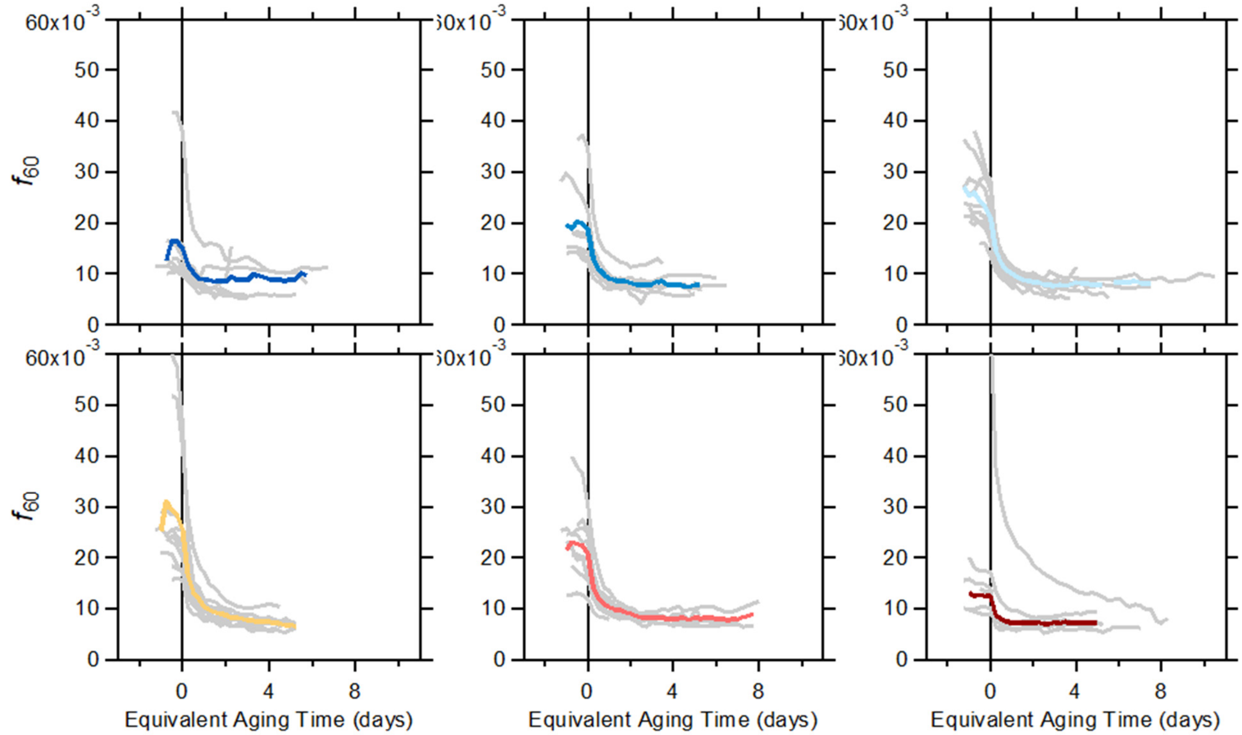

Figure S8. Relationship between the AMS f_{60} and the equivalent atmospheric aging time for each SSA classification. Individual burns are shown as gray lines, and the average for each SSA class as the colored line.

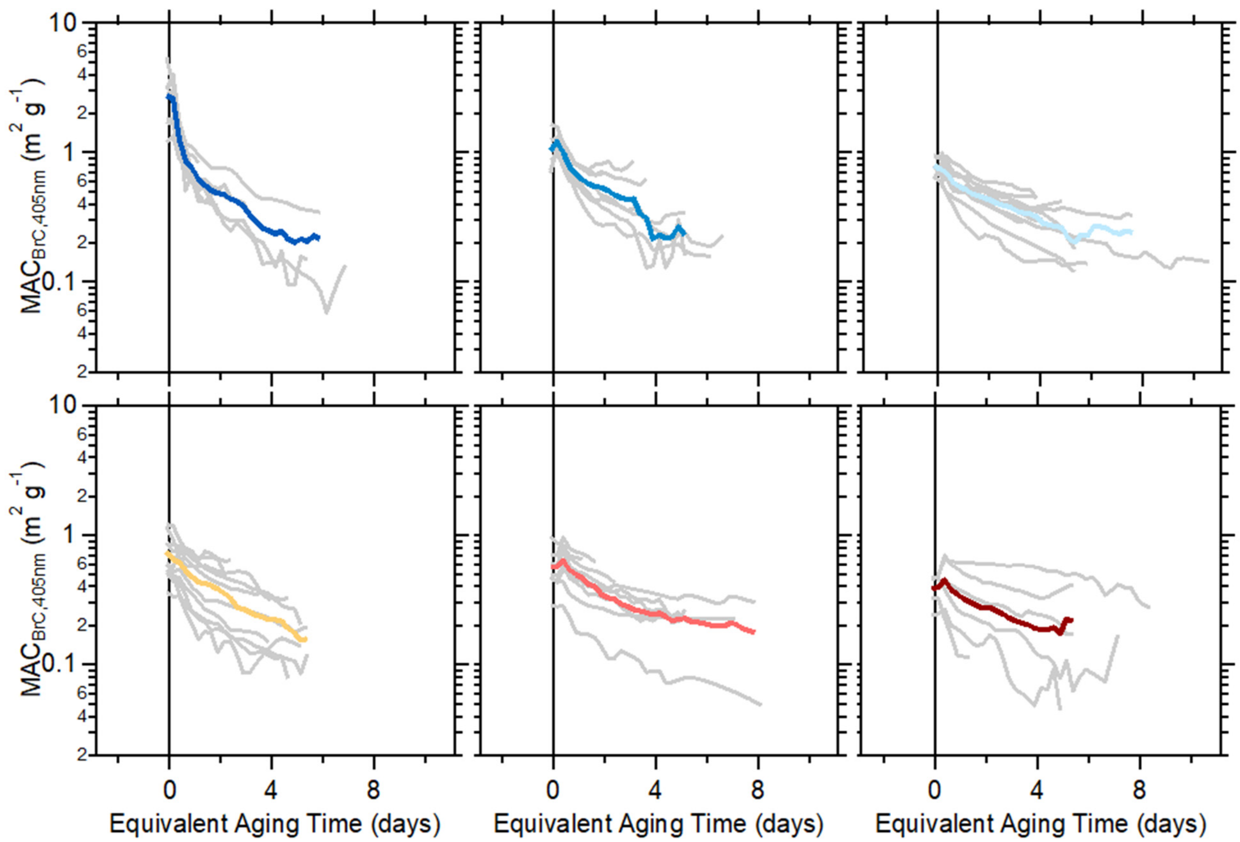

Figure S9. Relationship between the MAC_{BrC} at 405 nm and the equivalent atmospheric aging time for each SSA classification. Individual burns are shown as gray lines, and the average for each SSA class as the colored line.

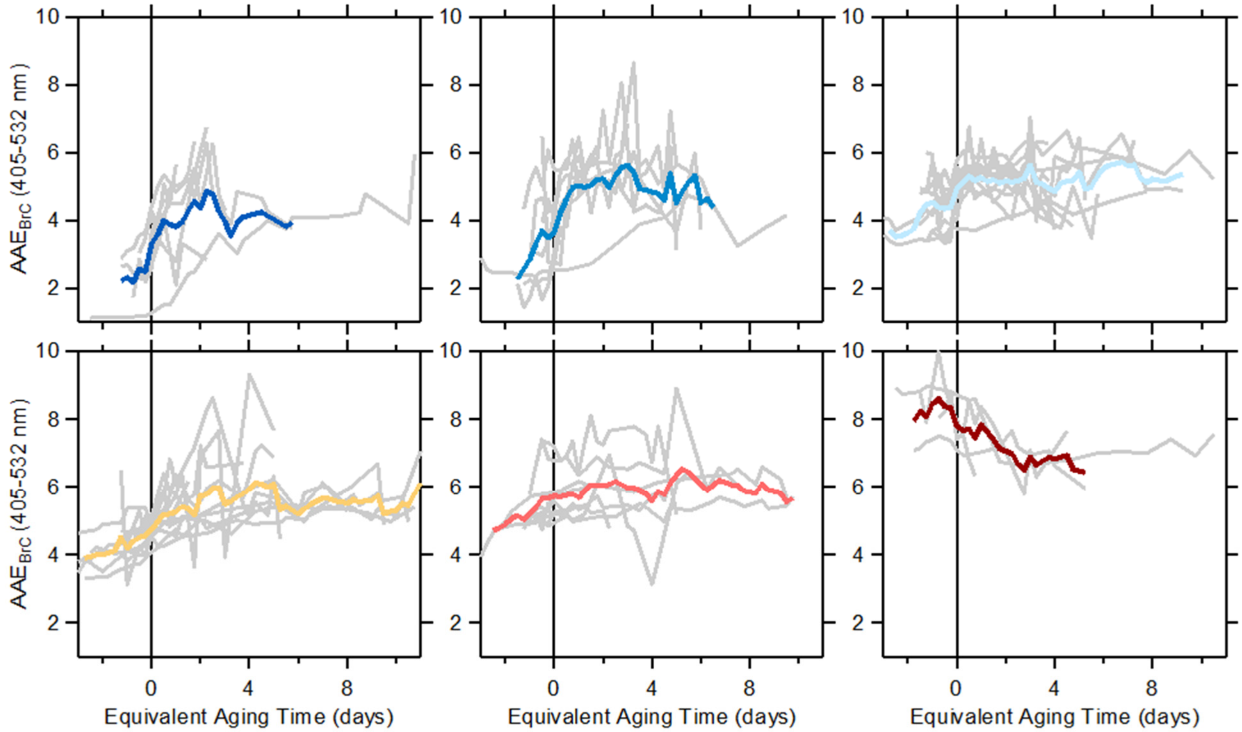

Figure S10. Relationship between the AAE_{BrC} for the 405-532 nm pair and the equivalent atmospheric aging time for each SSA classification. Individual burns are shown as gray lines, and the average for each SSA class as the colored line. Top row, left-to-right: class 1-3. Bottom row, left-to-right: class 4-6.

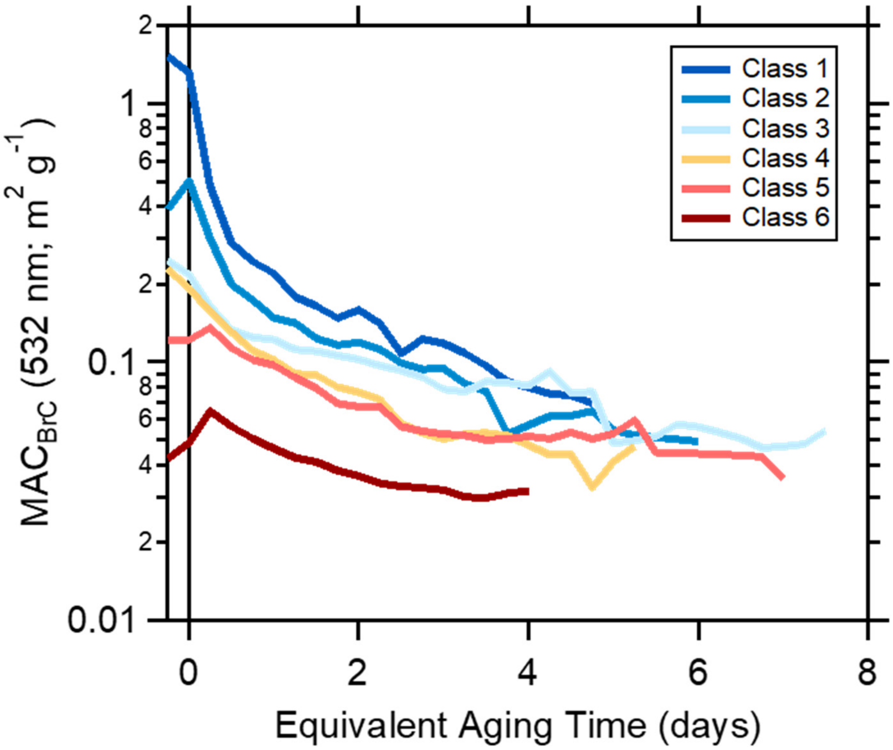

Figure S11. Influence of photochemical aging on MAC_{BrC} at 532 nm. The equivalent aging time assumes [OH] = 1.5 x 10^6 molecules/cm^3. The averages for each SSA classification are shown.

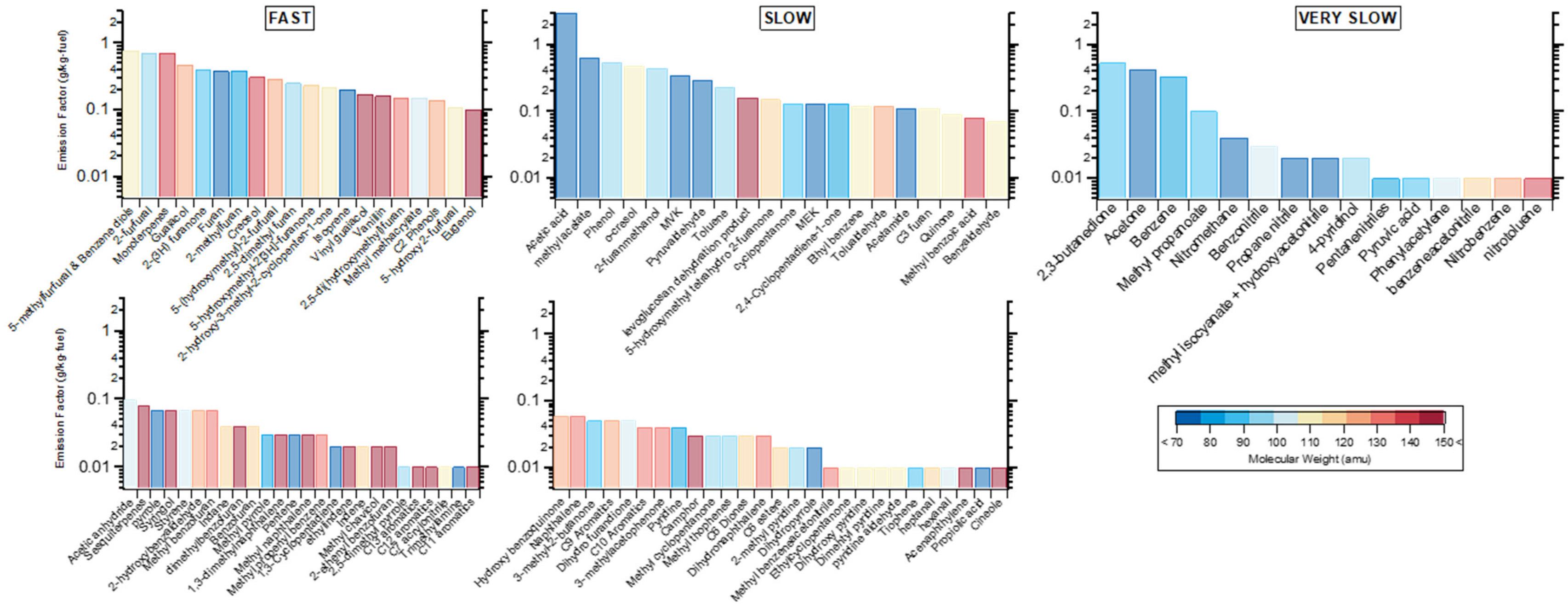

Figure S12. NMOG having MW > 50 amu, grouped into fast reacting, slow reacting and very slow reacting species. For each group, the NMOG are shown ordered according to the overall average emission factors, and are colored by their MW. Data are from Koss et al. (2018).

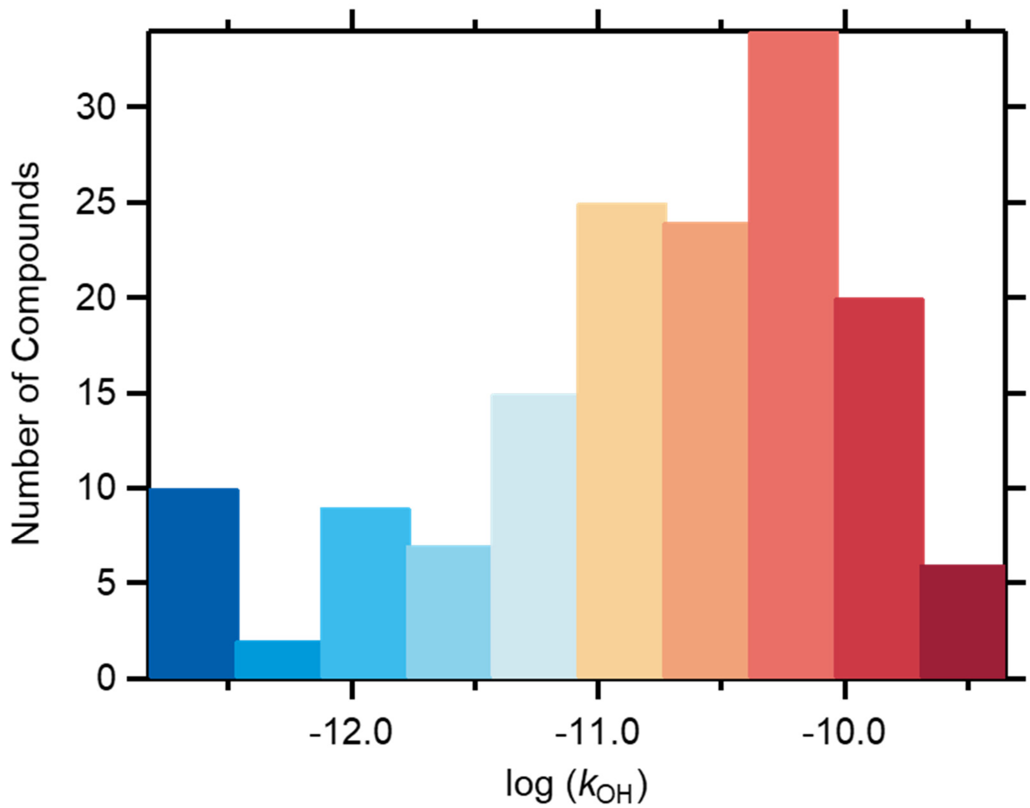

Figure S13. Histogram of rate coefficients for the NMOG having MW > 50 amu, as measured by Koss et al. (2018).

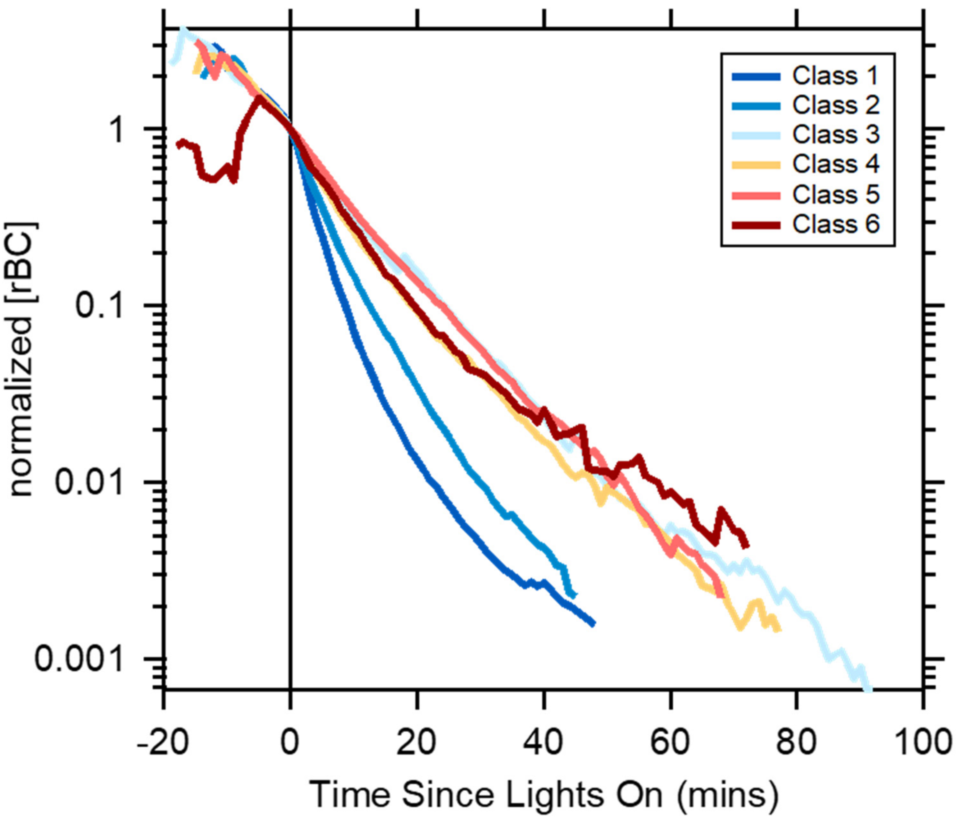

Figure S14. Normalized rBC concentration as a function of experiment time, averaged for each SSA classification. Results for each experiment are shown in **Figure S15**.

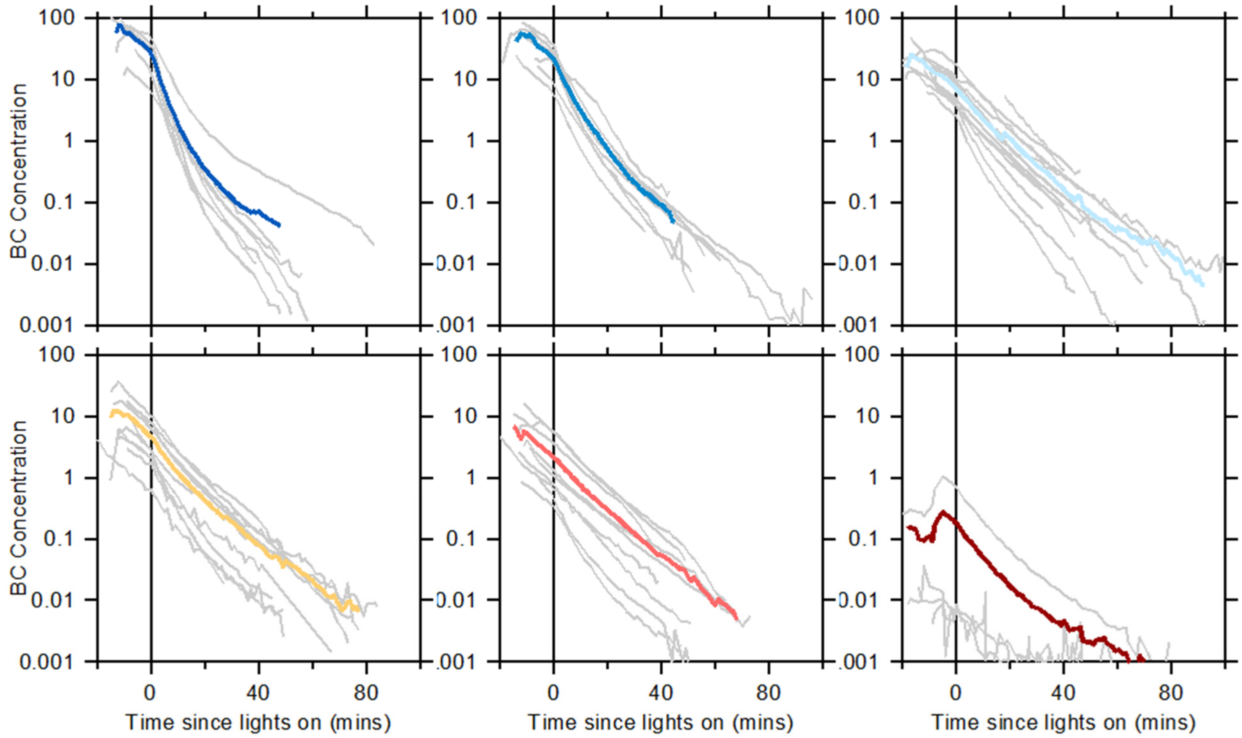

Figure S15. Normalized rBC concentration as a function of experiment time, with individual experiments shown as gray lines and the averages for each SSA classification as colored lines.

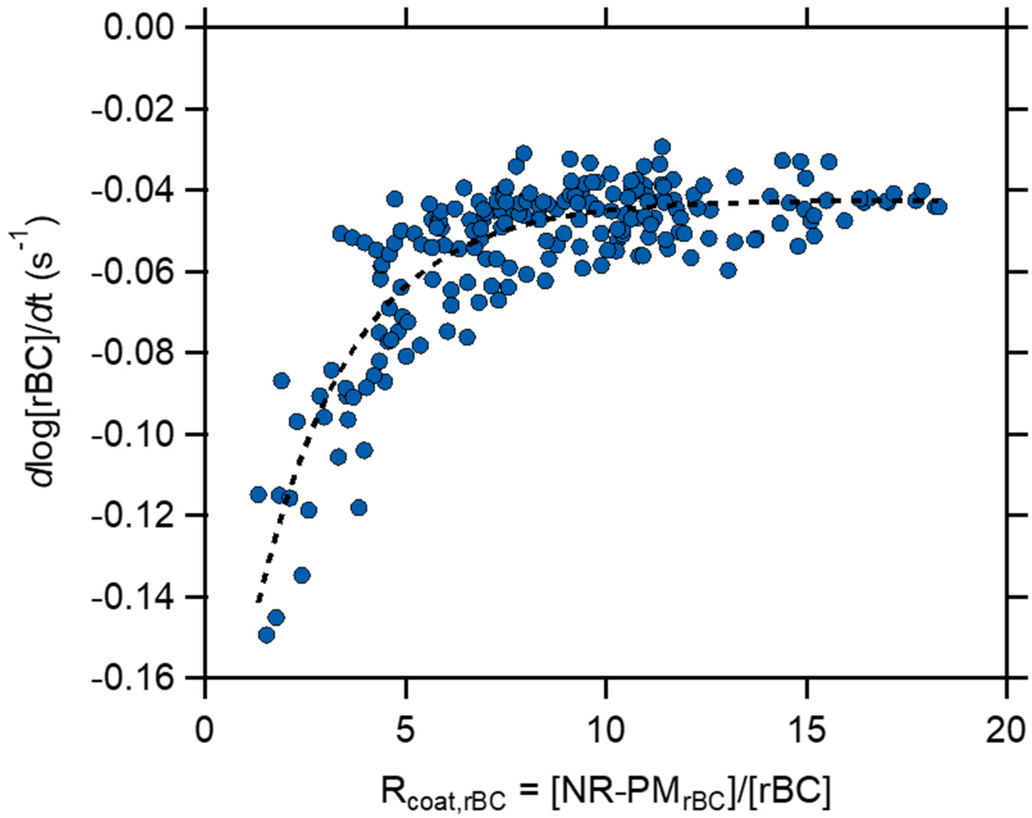

Figure S16. Observed loss rate of refractory BC as a function of the coating-to-core mass ratio. The data are fit using an exponential function, with -dlog[rBC]/dt = -0.0424 – 0.172·exp(-0.419·$R_{coat,rBC}$).

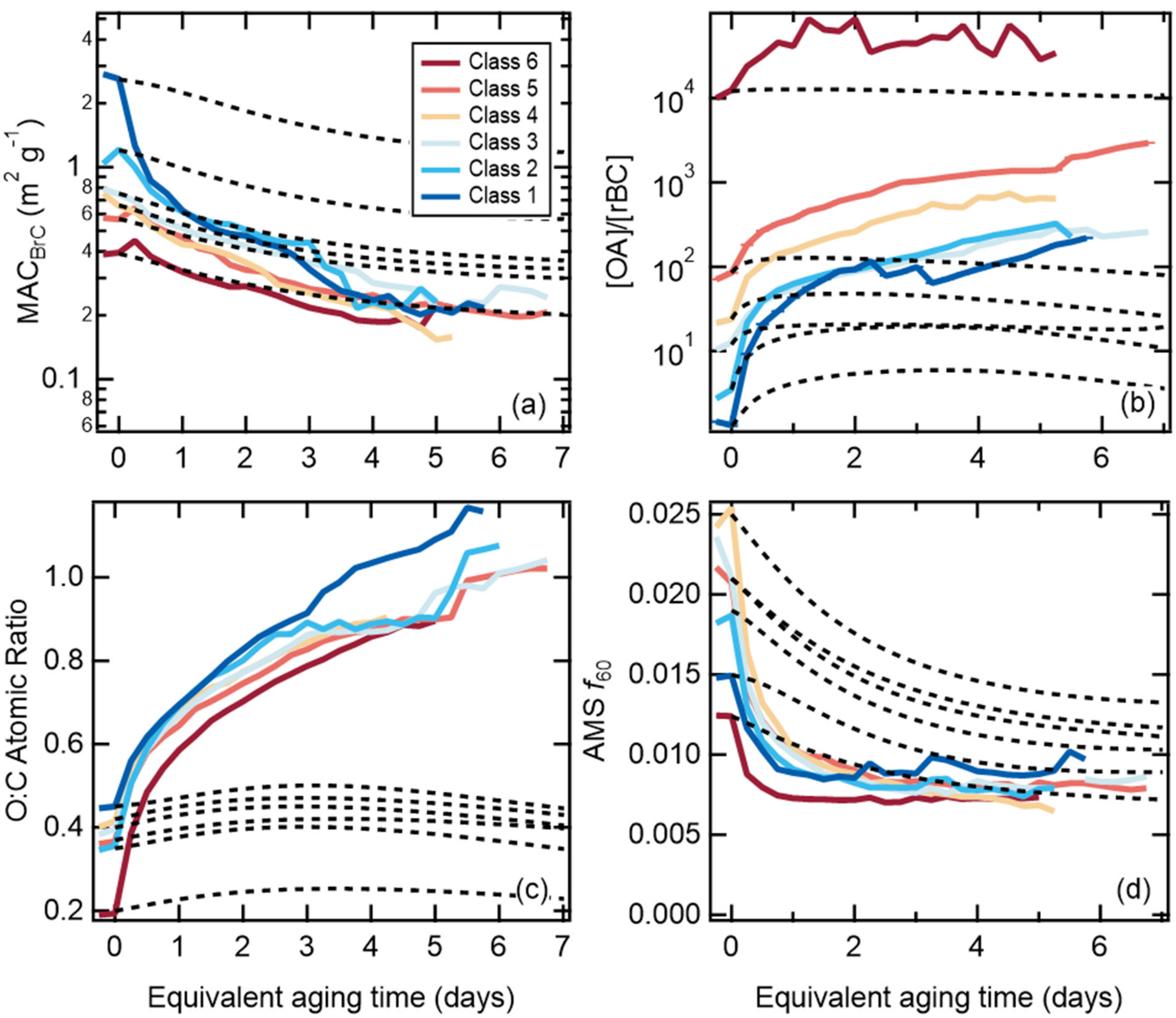

Figure S17. Comparison between observations (solid lines) and model results when only heterogeneous oxidation is included, i.e. no SOA (dashed lines). Results shown for values of the (a) MAC_{BrC}, (b) the [OA]/[rBC] ratio, (c) the O:C atomic ratio, and (d) the AMS f_{60} versus equivalent photochemical aging time (assuming [OH] = 1.5 x 10^6 molecules cm^{-3}), with results shown for each SSA class. The increase in the modeled [OA]/[rBC], despite there being no SOA formation in this model formulation, results from faster loss of OA that is internally mixed with rBC compared with the OA that is externally mixed.

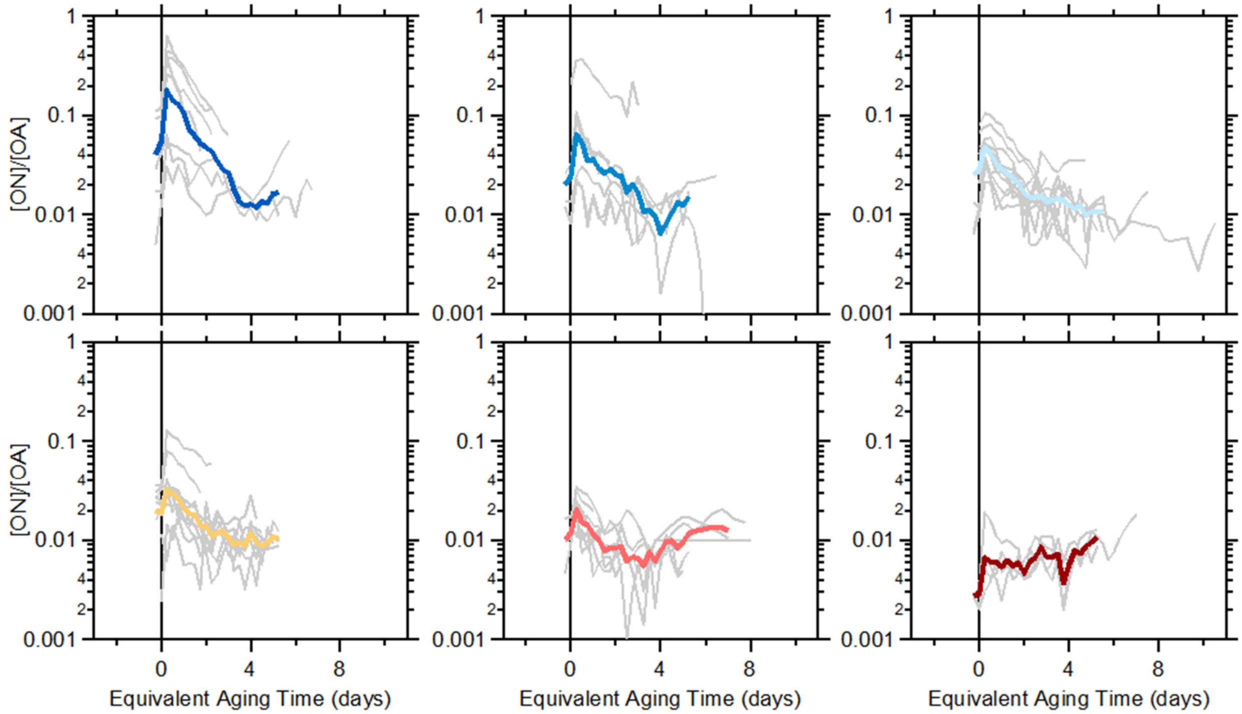

Figure S18. Dependence of the organic nitrate-to-total OA ratio on equivalent aging time for the different SSA classes. Individual burns are shown as gray lines, and the average for each SSA class as the colored line. Top row, left-to-right: class 1-3. Bottom row, left-to-right: class 4-6.

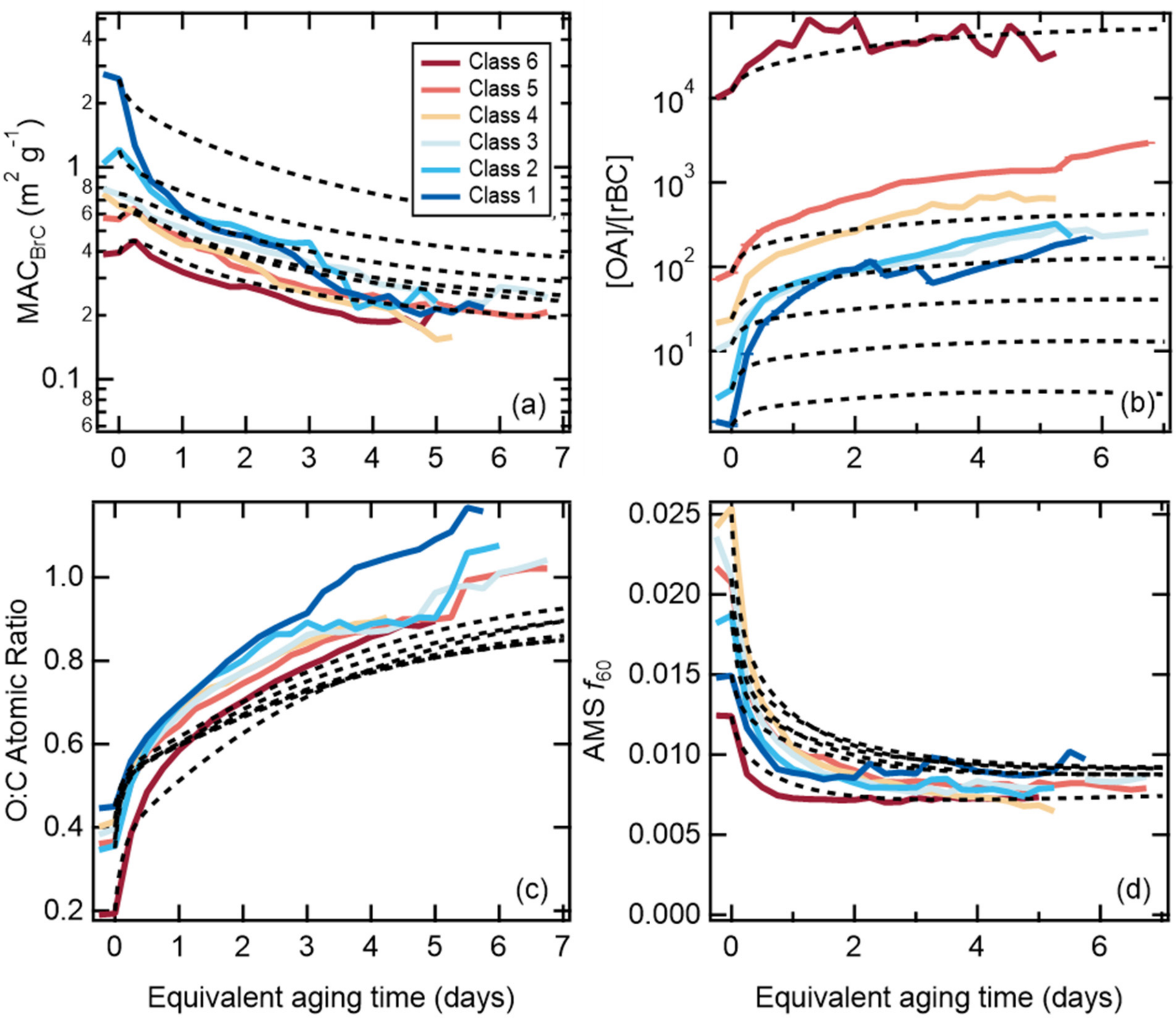

Figure S19. Same as **Error! Reference source not found.**, but where dilution is turned off entirely for both gases and particles. This corresponds to an "atmospheric" simulation.

1.3 Supplemental Tables

Table S1. Fuel types used.

Fuel Types*	
bear grass	lodgepole pine, mixed
ceanothus	lodgepole pine, canopy
chaparral (chamise), canopy	lodgepole pine, litter
chaparral (manzanita), canopy	Peat, Kalimantan
Douglas fir, mixed	ponderosa pine, mixed
Douglas fir, canopy	ponderosa pine, canopy
Douglas fir, litter	ponderosa pine, litter
Douglas fir, rotten log	ponderosa pine, rotten log
Engelmann spruce, mixed	rice straw
Engelmann spruce, canopy	sagebrush
Engelmann spruce, duff	subalpine fir, mixed
Engelmann spuce, Fish Lake, canopy	subalpine fir, canopy
Excelsior	subalpine fir, duff
Excelsior (poplar)	subalpine fir, litter
jeffrey pine, duff	subalpine fir
juniper, canopy	untreated lumber
loblolly pine, litter	yak dung

*Further details on each fuel type, including the particular mix for mixed-type burns, elemental composition, and moisture content are available on the NOAA FIREX project website at

Table S2. Instruments sampling from the mini chamber.

Instrument	Property Measured
	Particles
UCD CRD-PAS	Light absorption and dry/humidified light extinction at 405 nm and 532 nm
PASS-3	Light absorption and scattering at 781 nm
CAPS-SSA	Light extinction and scattering at 630 nm
HR-ToF-AMS	Bulk particle non-refractory composition and concentration for PM_1
SP-AMS	rBC-containing particle composition and concentration for PM_1
SP2	rBC concentrations and size distributions
SEMS	Mobility size distributions (10-1200 nm)
	Gases
Ozone monitor	O_3 concentrations
PTR-ToF-MS	Select non-methane organic gases
I^--CIMS	Select non-methane organic gases (not used here)
CO_2	CO_2 concentrations
RH probe	Relative humidity

Table S3. Fuels by particle Class.

Class	Fuel	SSA range	Log([OA]/[BC]) range
Class 1	Chaparral, canopy, litter (pine), building materials, excelsior	0.23-0.43	-0.52 – 0.38
Class 2	Manzanita, Sage, litter (fir)	0.43-0.60	0.18 – 0.61
Class 3	Pine, fir, litter, canopy, juniper	0.60-0.74	0.82 – 1.3
Class 4	Pine, fir, canopy, rotten log, ceonothos	0.74-0.87	0.92 – 1.74
Class 5	Canopy (pine), rice, bear grass, duff	0.87-0.93	1.49 – 2.16
Class 6	Rotten log, duff, peat, dung	0.93-1.00	2.63 – 2.02

Table S4. Summary of conditions for literature brown carbon aging experiments.

Reference	Aging method/notes	Fuel type/burning notes
Martinsson et al. (2015)	Aging of smoke in oxidation flow reactor (potential aerosol mass reactor); t_{OH} = 8.3 days	Birch; Combustion in a natural-draft conventional wood stove; likely class 1 to class 3 particles
Saleh et al. (2013)	Photochemical aging of smoke in 7 m^3 chamber for t_{OH} ~ a few hours; aging of pine likely > oak	Pocosin pine and oak; combustion at Missoula fire lab; likely class 1 particles
Zhong and Jang (2014)	Photochemical aging of smoke in a 104 m^3 outdoor chamber using natural sunlight; t_{OH} = a few hours; continual characterization	Hickory hardwood; Smoldering combustion; likely class 5
Kumar et al. (2018)	Photochemical aging of smoke in an 8 m^3 chamber; t_{OH} up to a day; Interpolate their observations to 405 nm	Beechwood; combustion in a residential wood stove; likely class 1
Sumlin et al. (2017)	Heterogeneous OH aging in an oxidation flow reactor (potential aerosol mass reactor); t_{OH} = 1, 3.5, 4.5 days	Alaskan peak; smoldering; likely class 6
Wong et al. (2017)	Photolytic aging (300-400 nm) of water-soluble and water-insoluble (methanol) extracts in a photoreactor; up to 130 h; photolysis of solutions	Cherry hardwood; Controlled pyrolysis; likely class 6, although measurements of suspended particles not available
Lee et al. (2014)	Photolytic aging (275-390 nm) of aqueous extracts; photolysis of solutions	SOA produced from naphthalene + OH
Fleming et al. (2020)	Photolytic aging (300-400 nm) of particles on filters; absorption by individual chromophores or total particles measured	Variety of fuels from FIREX, comprising different species and ecosystem components; range of particle classes likely

Fleming, L. T., Lin, P., Roberts, J. M., Selimovic, V., Yokelson, R., Laskin, J., Laskin, A., and Nizkorodov, S. A.: Molecular composition and photochemical lifetimes of brown carbon chromophores in biomass burning organic aerosol, Atmos. Chem. Phys., 20, 1105-1129, https://doi.org/10.5194/acp-20-1105-2020, 2020.

Kumar, N. K., Corbin, J. C., Bruns, E. A., Massabó, D., Slowik, J. G., Drinovec, L., Močnik, G., Prati, P., Vlachou, A., Baltensperger, U., Gysel, M., El-Haddad, I., and Prévôt, A. S. H.: Production of particulate brown carbon during atmospheric aging of wood-burning emissions, Atmos. Chem. Phys., 2018, 17,843-817,861, https://doi.org/10.5194/acp-18-17843-2018, 2018.

Lee, H. J., Aiona, P. K., Laskin, A., Laskin, J., and Nizkorodov, S. A.: Effect of Solar Radiation on the Optical Properties and Molecular Composition of Laboratory Proxies of Atmospheric

Brown Carbon, Environmental Science & Technology, 48, 10217-10226, https://doi.org/10.1021/es502515r, 2014.

Martinsson, J., Eriksson, A. C., Nielsen, I. E., Malmborg, V. B., Ahlberg, E., Andersen, C., Lindgren, R., Nyström, R., Nordin, E. Z., Brune, W. H., Svenningsson, B., Swietlicki, E., Boman, C., and Pagels, J. H.: Impacts of Combustion Conditions and Photochemical Processing on the Light Absorption of Biomass Combustion Aerosol, Environmental Science & Technology, 49, 14663-14671, https://doi.org/10.1021/acs.est.5b03205, 2015.

Saleh, R., Hennigan, C. J., McMeeking, G. R., Chuang, W. K., Robinson, E. S., Coe, H., Donahue, N. M., and Robinson, A. L.: Absorptivity of brown carbon in fresh and photo-chemically aged biomass-burning emissions, Atmospheric Chemistry and Physics, 13, 7683-7693, https://doi.org/10.5194/acp-13-7683-2013, 2013.

Sumlin, B. J., Pandey, A., Walker, M. J., Pattison, R. S., Williams, B. J., and Chakrabarty, R. K.: Atmospheric Photooxidation Diminishes Light Absorption by Primary Brown Carbon Aerosol from Biomass Burning, Environmental Science & Technology Letters, 4, 540-545, https://doi.org/10.1021/acs.estlett.7b00393, 2017.

Wong, J. P. S., Nenes, A., and Weber, R. J.: Changes in Light Absorptivity of Molecular Weight Separated Brown Carbon Due to Photolytic Aging, Environmental Science & Technology, 51, 8414-8421, https://doi.org/10.1021/acs.est.7b01739, 2017.

Zhong, M., and Jang, M.: Dynamic light absorption of biomass-burning organic carbon photochemically aged under natural sunlight, Atmospheric Chemistry and Physics, 14, 1517-1525, https://doi.org/10.5194/acp-14-1517-2014, 2014.